Reconstruction of Thermal Protection System Aeroheating Using a Green's Function Approach

Kenneth McAfee* and Oded Rabin†
University of Maryland, College Park, MD 20742

Hannah S. Alpert‡
NASA Ames Research Center, Moffett Field, CA 94035

Inverse heat transfer (IHT) techniques are often used to reconstruct the surface heating conditions on spacecraft thermal protection systems (TPS) during atmospheric entry. Current IHT techniques for entry spacecraft applications, however, demand substantial computational resources, and are impractical for analyses such as uncertainty quantification and real-time health monitoring. In this paper, a Green's function sensor fusion approach is used to reconstruct the TPS surface aeroheating conditions on experimental spaceflight and ground test systems from collocated temperature and heat flux sensors embedded in the TPS. The algorithm leverages Green's functions to model the heat conduction within the spacecraft TPS and stabilizes the recovery of the surface heat flux boundary condition using the direct heat flux sensor measurement. The algorithm is validated using arc-jet ground test data and applied to the reconstruction of the Mars 2020 backshell heating during Martian atmospheric entry. The performance of the algorithm is benchmarked against a current state-of-the-art IHT framework, FIAT_Opt. The Green's function-based reconstruction algorithm recovers the net hot-wall heat flux absorbed by the TPS and the incident heat flux from the atmospheric entry environment in close agreement with FIAT_Opt. Notably, computation of the surface heating conditions is completed in three orders of magnitude less time with the Green's function sensor fusion approach using a consumer-grade PC, versus with FIAT_Opt running on a high-performance computer cluster. The efficiency of the algorithm is leveraged to compute the uncertainty contributions of input parameters to the total uncertainty of reconstructed Mars 2020 backshell heating conditions for the full atmospheric entry heat pulse. The sensitivity analysis uncovers that, at different times throughout the entry heat pulse, uncertainties in the TPS specific heat, thermal conductivity, and emissivity are all dominant drivers of the reconstruction uncertainty. These results demonstrate Green's functions and sensor-fusion techniques as promising IHT approaches to reconstruct atmospheric entry environments from TPS-embedded measurements, and highlight how these techniques may give access to post-flight analyses previously hindered by the prohibitive cost of current methods.

I. Nomenclature

A	=	Cole-Hopf transformation constant
C, C_0	=	proportionality constants between hot- and cold-wall heat flux values
C_p	=	specific heat $(J/(kg \cdot K))$
$f(\theta)$	=	Cole-Hopf transformation
$\hat{f}$	=	Galerkin basis functions
$g(x,t)$	=	internal source term (W/m^3)
$g'(x,t)$	=	modified internal source term (W/m^3)
$g_{tot}(x,t)$	=	integrated effects of temperature-dependent material properties
G	=	Green's function $(1/m)$

*Graduate Student, Department of Aerospace Engineering, Student Member AIAA
†Associate Professor, Department of Materials Science and Engineering, Institute for Research in Electronics and Applied Physics
‡Systems Engineer, Entry Systems and Vehicle Development Branch

k	=	thermal conductivity $(W/(m \cdot K))$
L	=	thickness (m)
L_2	=	2nd derivative finite difference operator
N	=	basis function order
N_s	=	number of Monte Carlo samples
q	=	heat flux $\left(W/m^2\right)$
x	=	general position coordinate (m)
x_0	=	dummy position coordinate (m)
$\tilde{T}$	=	absolute temperature (K)
T	=	temperature relative to initial conditions or a reference temperature (K)
θ	=	transformed temperature
t	=	time (s)
τ	=	dummy time variable (s)
α	=	thermal diffusivity $\left(m^2/s\right)$
α_s	=	absorptivity
χ	=	char volume fraction
ϵ	=	emissivity
$\lambda_2, \lambda_2^{(0)}$	=	regularization coefficients
Λ	=	Eigenvalues
μ	=	mean
ϕ	=	Eigenfunctions
ψ	=	Eigenvectors
ρ	=	density $\left(kg/m^3\right)$
σ	=	standard deviation
σ_{SB}	=	stefan-boltzmann constant $\left(W/\left(m^2 \cdot K^4\right)\right)$
τ_{HFS}	=	heat flux sensor response time (s)

II. Introduction

Recent space exploration missions have featured extensive thermal instrumentation suites embedded in the vehicle thermal protection system (TPS) to measure atmospheric entry heat rates and evaluate TPS performance. These instrumentation suites have contained combinations of direct Schmidt-Boelter-type heat flux sensors, thermocouple plugs with one or more temperature probes embedded at various depths, and discrete temperature sensors [1–3]. Post-flight efforts to reconstruct the atmospheric entry conditions using measurements from each sensor type have leveraged various methodologies, including computational fluid dynamics (CFD) simulations and inverse heat transfer (IHT) solvers [4–6]. IHT techniques—using measurements from embedded temperature probes to reconstruct the surface heat flux boundary condition—are most often used for post-flight assessment of the TPS thermal loading. In addition to recovering the TPS surface heating conditions on atmospheric entry spacecraft, these methods have aided in the interpretation of measurements from direct heat flux sensors by providing more accurate wall boundary conditions for CFD-based reconstruction schemes [6]. Furthermore, for ground testing applications, IHT-based methods present a valuable diagnostic tool to evaluate the heating conditions experienced by a test article whose surface is neither at an adiabatic-wall or cold-wall state, and cannot be directly inferred from cold-wall calorimetry-based calibration. While advantageous for numerous in-flight and ground test applications, however, current state-of-the-art IHT and CFD-based aerothermal reconstruction methodologies demand substantial computational resources. These techniques, which rely on the use of a discrete mesh and time-marching finite volume or finite element schemes, require the whole-domain material response solution at each time step [7]. For more intensive analyses, such as uncertainty quantification, or time-sensitive processes, such as real-time health monitoring, current IHT methods become impractical to implement, even with access to modern computational tools [5]. As such, there is a need for alternative computational methods that are more efficient and optimized for the aerothermal environment reconstruction end use-case.

Green's function based approaches offer a computationally efficient framework well-suited to address the drawbacks associated with current IHT methods for atmospheric entry applications. In prior work, a Green's function sensor fusion approach was developed for efficient reconstruction of the hot-wall TPS surface heating conditions using collocated heat flux sensor and temperature-probe measurements [8]. The approach models the subsurface heat conduction in the TPS surrounding the heat flux sensor using the Green's function formulation and leverages the direct heat flux sensor

measurement to stabilize the recovery of the heat flux boundary condition on the TPS surface. In contrast to prevailing time-marching IHT methods [5, 7], the mesh-free Green's function approach models the material response only at a single location (i.e., the temperature measurement location), but for the entire time series at once [9–11]. Green's function-based approaches are thus inherently optimized for IHT problems and require substantially less computational overhead than other methods. In this paper, the Green's function IHT sensor fusion approach (herein named the *hot-wall heat flux reconstruction algorithm*) is validated using ground-test data and applied to the post-flight reconstruction and uncertainty quantification of the Mars 2020 backshell aeroheating environment. The approach is benchmarked against the current state-of-the-art IHT code for spacecraft TPS applications, FIAT_Opt. The following sections are outlined as follows: Section III details the model analogue used to represent the TPS-embedded heat flux and temperature sensors in experimental spaceflight and ground test systems. Section IV provides an overview of the reconstruction algorithm and methodology to solve for individual heating terms within the net surface energy balance. The reconstruction algorithm is then used to reconstruct TPS surface heating conditions from measurements obtained through ground testing in an arc-jet facility (Section V.A) as well as measurements from the Mars 2020 atmospheric entry vehicle (Section V.B). The results from a full-flight uncertainty quantification of the Mars 2020 reconstructed heating conditions are presented in Section VI.

III. Measurement System Overview

The Mars 2020 atmospheric entry spacecraft flew an extensive suite of TPS-embedded thermal instrumentation as part of the Mars Entry Descent and Landing Instrumentation 2 (MEDLI2) program [1]. Among these were two pairs of collocated thermocouple (TC) plugs and heat flux sensors located on the backshell shoulder region: the MTB01/MTB07 TC plug/heat flux sensor pair, embedded in the wind-side region of the backshell, and the MTB02/MTB08 sensor pair, embedded in the lee-side region of the backshell. Both sensor pairs are highlighted in Fig. 1. In the flight configuration, the distance between paired heat flux sensors and TC plugs was approximately 10 cm and 18 cm for the MTB01/MTB07 and MTB02/MTB08 sensor pairs, respectively [1]. Within each TC plug, the shallowest TC was placed at a nominal depth of 0.254 cm from the external TPS surface [5]. In the region of the sensors, the nominal thickness of the TPS was 1.27 cm [12]. During atmospheric entry, measurements from the TC plugs and heat flux sensors were sampled at a rate of 8 Hz and 16 Hz, respectively.

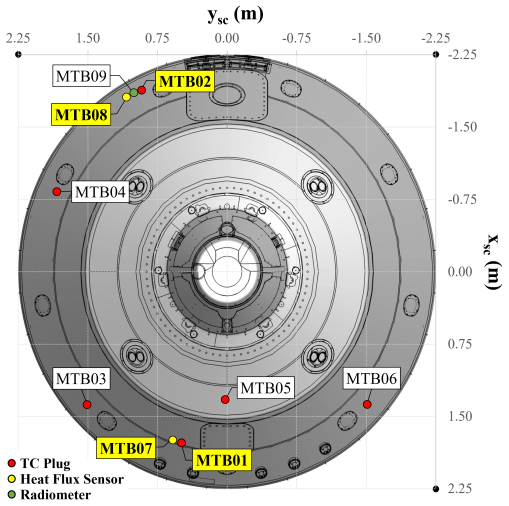

Fig. 1 Schematic of the Mars 2020 backshell showing the MEDLI2 instrumented TC plug, heat flux sensor, and radiometer locations (adapted from [1]). Highlighted sensor labels indicate those used in this work.

A schematic of the model system used to represent the as-flown sensor pairs and analogous ground test configurations is shown in Fig. 2. The model system represents the heat flux sensor (HFS) and TC plug as separate 1D domains with thickness $L = 1.27$ cm, perfectly insulated from each other. In the TC plug domain, the temperature probe is placed in the TPS at a depth of $L - x_T = 0.254$ cm from the external surface. The external surfaces of the TC plug and heat flux sensor are exposed to the aeroheating environment. The heat flux sensor measures an augmented cold-wall

heat flux q_{CW} due to passive thermal management via a full-thickness copper heat sink. The net hot-wall heat flux q_{HW} absorbed by the TPS in the TC plug is comparatively lower as a result of the strong radiative emission and lower convective heat rates at the hot-wall TPS surface. The internal surfaces of the domains are modeled as fully insulating. This approximation will result in an underprediction of q_{HW}, as the flight-relevant material stack-up includes other supporting components in contact with the internal surface of the TPS. However, preliminary studies comparing a constant temperature internal surface scenario, which overpredicts q_{HW}, and an insulating internal surface scenario, which underestimates q_{HW}, showed minimal differences between solutions. Thus, any errors associated with the choice in boundary condition are presumed to be small.

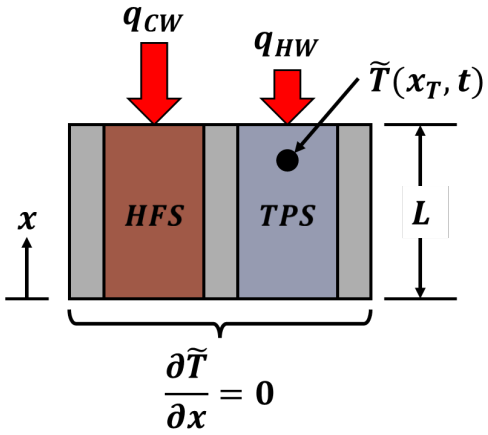

Fig. 2 Model system schematic. The heat flux sensor and TC plug are modeled as separate 1D domains. The external surface (top) is exposed to the aeroheating environment and the internal surface (bottom) is insulated. In the TC plug domain, the temperature probe is embedded within the TPS near the external surface.

IV. Hot-Wall Heat Flux Reconstruction Algorithm

The objective of the hot-wall heat flux reconstruction algorithm is to recover the net hot-wall heat flux absorbed by the TPS q_{HW} solely using the TPS temperature time history and local cold-wall heat flux q_{CW}, measured by the embedded temperature probe and collocated heat flux sensor, respectively. A brief overview of the reconstruction algorithm, detailed comprehensively in [8], is given here. The reconstruction approach consists of two steps. First, a Green's function formulation is developed to efficiently model the transient heat conduction within the TPS at the temperature measurement location. Due to the strong temperature-dependence of the thermophysical properties of TPS materials, the governing heat conduction equation is linearized via the Cole-Hopf transform. In the second step, the Green's function representation of the TPS thermal history is inverted to recover the net hot-wall heat flux absorbed at the TPS surface, leveraging the collocated heat flux sensor to stabilize the ill-posed system.

A. Nonlinear Heat Conduction and Green's Function Formalism

The temperature distribution within the TPS solid is governed by the heat conduction equation

$$\rho C_p\left(\tilde{T}\right)\frac{\partial \tilde{T}}{\partial t} = \frac{\partial}{\partial x}\left[k\left(\tilde{T}\right)\frac{\partial \tilde{T}}{\partial x}\right] + g(x,t) \tag{1}$$

Following [8], Eq. (1) is linearized by expanding $\tilde{T} = T + \tilde{T}_0$ and introducing the Cole-Hopf transformation $T = f(\theta)$, yielding

$$\frac{1}{\alpha_0}\frac{\partial \theta}{\partial t} - \frac{\partial^2 \theta}{\partial x^2} = \frac{g'(x,t)}{A} \tag{2}$$

where

$$\frac{g'(x,t)}{A} = \frac{\alpha_T(T)}{\alpha_0}\frac{\partial^2 \theta}{\partial x^2} + \frac{\alpha_0 + \alpha_T(T)}{\alpha_0}\frac{g(x,t)}{A} \tag{3}$$

In Eq. (2) and (3), A is a constant of integration from the Cole-Hopf transformation [13] and the thermal diffusivity is expanded relative to a reference value $\alpha_0 = \alpha(\tilde{T}_0)$

$$\alpha(\tilde{T}) = \alpha_0 + \alpha_T(T) \tag{4}$$

Within the Green's function formalism, the transformed temperature at the sensor location is given by the sum of two integral terms which capture the effects of the hot-wall heat flux boundary condition q_{HW} at the TPS surface and the internal source term g' from Eq. (2)

$$\theta(x,t) = -\int_0^t \frac{\alpha_0}{A} q_{HW}(\tau) G\left(x,t,L,\tau\right)\, d\tau + \int_0^t \int_0^L \frac{\alpha_0}{A} g'\left(x_0,\tau\right) G\left(x,t,x_0,\tau\right)\, dx_0\, d\tau \tag{5}$$

where Green's function $G\left(x,t,x_0,\tau\right)$ is constructed using the Galerkin method. Adapted from [9] and [10],

$$G\left(x,t,x_0,\tau\right) = \sum_{n=1}^{N} \phi_n(x)\phi_n(x_0) e^{-\Lambda_{n,n}(t-\tau)} \tag{6}$$

In Eq. (6), $\Lambda_{n,n}$ represents the eigenvalue accompanying each eigenfunction ϕ_n. The eigenfunctions are approximated using an N-ordered sum of scaled basis functions $\hat{f}$

$$\phi_n = \sum_{j=1}^{N} \psi_{j,n} \hat{f}_j \tag{7}$$

In Eq. (7), basis functions $\hat{f}_j$ are required to satisfy the homogeneous boundary conditions imposed on the system. For the 1D heat conduction system used in this work, the basis functions are a set of polynomials with even behavior about $x = 0$

$$\hat{f}_j = x^{2j-2} \tag{8}$$

for $j = \{1, \ldots, N\}$. Basis functions are then scaled by the eigenvector ψ_n accompanying the respective eigenfunction ϕ_n. Eigenvalues $\Lambda_{n,n}$ and eigenvectors ψ_n are calculated using the approach described in [14].

B. Recovery of the Hot-Wall Heat Flux

In the second step of the reconstruction algorithm, the net hot-wall heat flux is recovered from the Green's function formulation of the TPS thermal response. The net hot-wall heat flux is first isolated from all other quantities in Eq. (5). For tractability, the integrated source term is represented by the parameter $g_{tot}(x,t)$

$$g_{tot}(x,t) = \int_0^t \int_0^L \frac{\alpha_0}{A} g'\left(x_0,\tau\right) G\left(x,t,x_0,\tau\right)\, dx_0\, d\tau \tag{9}$$

Equation (5) is then rearranged and expressed as

$$\theta(x,t) - g_{tot}(x,t) = -\int_0^t \frac{\alpha_0}{A} q_{HW}(\tau) G\left(x,t,L,\tau\right)\, d\tau \tag{10}$$

In Eq. (10), the left-hand-side consists purely of measured quantities and contributions of the integrated source term on the measured quantities. For measurements sampled at a finite rate, Eq. (10) is recast as a discrete linear system [11]

$$\{\theta\} - \{g_{tot}\} = -\frac{\alpha_0}{A}\left[G\right]\{q_{HW}\} \tag{11}$$

Inversion of the linear system in Eq. (11) is ill-posed and prone to instabilities. In prior work, the collocated heat flux sensor measurement was used to stabilize the direct inversion of Eq. (11) by enforcing smoothness between the cold-wall heat flux—measured by the heat flux sensor— and the net hot-wall TPS heat flux time histories

$$q_{HW} = C(t) q_{CW} + C_0(t) \bar{q}_{CW} \tag{12}$$

where $C(t)$ is an unknown, smooth, time-varying function with a continuous 2nd derivative in time. An additional time-dependent coefficient $C_0(t)$ is incorporated in Eq. (12) to avoid singularities that occur in $C(t)$ when the ratio

q_{CW}/q_{HW} is small. The coefficient $C_0(t)$ scales the quantity $\bar{q}_{CW}$, which represents the average value of $\bar{q}_{CW}$ up to time $t + \tau_{HFS}$, where τ_{HFS} is the response time of the heat flux sensor. Using Eq. (12), Eq. (11) is recast as a function of $C(t)$ and $C_0(t)$

$$\{\theta\} - \{g_{tot}\} = -\frac{\alpha_0}{A}\,[G]\,[\text{diag}\,(q_{CW})\ \text{diag}\,(\bar{q}_{CW})]\begin{Bmatrix} C(t) \\ C_0(t) \end{Bmatrix} \tag{13}$$

where diag (q_{CW}) and diag $(\bar{q}_{CW})$ are square matrices with the time series q_{CW} and $\bar{q}_{CW}$, respectively, arranged along the diagonal elements. When the temperature probe and heat flux sensor are sampled at different rates, the measurements are first downsampled to match the size of each measurement time series. The solution of $C(t)$ and $C_0(t)$ is calculated by simultaneously minimizing the squared l^2-norms of the residual in Eq. (13) and the 2nd derivatives of $C(t)$ and $C_0(t)$ to enforce smoothness in $C(t)$ and $C_0(t)$.

$$\min\left\{\left\|\{\theta\} - \{g_{tot}\} + \frac{\alpha_0}{A}[G]\,[\text{diag}\,(q_{CW})\ \text{diag}\,(\bar{q}_{CW})]\begin{Bmatrix} C(t) \\ C_0(t) \end{Bmatrix}\right\|_2^2 + \left\|\begin{Bmatrix} \lambda_2 \\ \lambda_2^{(0)} \end{Bmatrix} \cdot \begin{bmatrix} L_2 \\ L_2 \end{bmatrix}\begin{Bmatrix} C(t) \\ C_0(t) \end{Bmatrix}\right\|_2^2\right\} \tag{14}$$

In Eq. (14) the regularization coefficients λ_2 and $\lambda_2^{(0)}$ tune the magnitude of the 2nd derivative penalty term, where L_2 is a discrete 2nd derivative finite difference operator acting on $C(t)$ and $C_0(t)$. Following the solution of $C(t)$ and $C_0(t)$, q_{HW} is recovered using Eq. (12).

In the simplest case, when the terms in Eq. (14) are not dependent on the thermal history of the TPS (i.e., constant material properties), the solutions for $C(t)$ and $C_0(t)$ can be accessed directly by differentiating Eq. (14). Often, however, g_{tot} is unknown, and must be calculated using iterative solutions of q_{HW}. The volumetric integration of g' in g_{tot} (Eq. (9)), which arises when temperature-dependent material properties or other non-linear energy generation phenomena are present, is the major computational burden in the reconstruction algorithm. In this work, a Gaussian quadrature scheme is used to approximate the volume integrals by calculating the integrand term in Eq. (9) at a small number ($\mathcal{O}(10)$) of discrete locations within the TPS [15, 16]. Equation (14) and Eq. (9) are then solved simultaneously, where the net hot-wall heat flux solution is used to calculate g' at the volume integration abscissas in g_{tot} via Eq. (3) and (5). For a measurement time series with 600 sample points, the reconstruction algorithm routinely converges in less than 3 seconds using a consumer-grade personal computer. By comparison, conventional time-marching-based IHT methods generate solutions for the same number of sample points in approximately 30 minutes, aided by state-of-the art computing clusters and significant code optimization [5].

C. Surface Energy Balance

In the reconstruction algorithm, the net hot-wall heat flux q_{HW} represents the heat flux conducted into the TPS solid. At the surface of the TPS, multiple heat transfer mechanisms contribute to q_{HW}. These terms are related to the net hot-wall heat flux q_{HW} via the surface energy balance

$$q_{HW} = q_{conv} + \alpha_s q_{rad} - \epsilon_s \sigma_{SB}(\tilde{T}_s^4 - \tilde{T}_\infty^4) \tag{15}$$

In the right-hand-side of Eq. (15), the first term represents the convective heat flux through the viscous boundary layer. The second term represents the absorbed heat flux from the shock layer radiation, where α_s is the absorptivity of the TPS surface and q_{rad} is the total hemispherical radiative flux incident on the TPS. The third term represents the radiative emission from the hot TPS, where ϵ_s is the emissivity of the TPS surface, σ_{SB} is the Stefan-Boltzmann constant, $\tilde{T}_s$ is the TPS surface temperature, and $\tilde{T}_\infty$ represents the background temperature. For heating values representative of the Mars 2020 atmospheric entry heat pulse, other phenomena such as surface recession and thermochemical ablation are assumed to have minimal contributions to the net surface energy balance on the backshell TPS, and will not be included in the current analysis.

Often of interest for entry spacecraft are the heat loads imposed by the aerothermal environment during atmospheric entry. These are represented by the first two terms on the right-hand-side of Eq. (15), the sum of which will be referred to as the incident heat flux q_{inc} hereafter. To recover q_{inc}, q_{HW} is corrected by the radiative emission from TPS surface, such that

$$q_{inc} = q_{HW} + \epsilon_s \sigma_{SB}(\tilde{T}_s^4 - \tilde{T}_\infty^4) \tag{16}$$

In Eq. (16), the surface temperature $\tilde{T}_s$ is calculated using Eq. (5), where Green's function is defined for a virtual temperature measurement at the TPS surface. Due to the strong dependence of emissivity on the formation of char

at the surface, pyrolysis and material decomposition must be considered. The TPS surface emissivity is defined as a function of both temperature and char volume fraction, χ [17]

$$\epsilon_s(\tilde{T}, \chi) = [1 - \chi]\frac{\rho_v}{\rho_s}\epsilon_v(\tilde{T}) + \chi\frac{\rho_c}{\rho_s}\epsilon_c(\tilde{T}) \tag{17}$$

where the subscripts v, c, and s represent properties corresponding to the fully virgin, fully charred, and partially charred composite TPS material, respectively. The char volume fraction is a function of the solid density ρ_s relative to the fully virgin and fully charred states

$$\chi = (\rho_s - \rho_v)/(\rho_c - \rho_v) \tag{18}$$

The decomposition of the TPS at the surface is modeled using an Arrhenius rate equation, as per [18], in which the time evolution of ρ_s is purely a function of the surface temperature time history. Once the state of the TPS surface is defined, q_{inc} is calculated via Eq. (16).

D. FIAT_Opt

To benchmark the performance of the hot-wall heat flux reconstruction algorithm, reconstructions of the TPS surface heating conditions will be compared to those generated using the state-of-the-art IHT code FIAT_Opt. FIAT_Opt, developed at NASA Ames, utilizes NASA's one-dimensional thermal energy transport modeling tool, the Fully Implicit Ablation and Thermal Response Analysis Program (FIAT) [19]. FIAT takes the aerothermal environment and aeroshell material stack-up as inputs, and outputs the thermal response of the material throughout its depth. In FIAT_Opt, the embedded temperature measurements and material stack-up are used instead as inputs, and the program adjusts the surface heating profile to minimize the difference between the in-depth FIAT temperature predictions and the input measurements. FIAT_Opt offers the user several options for minimization and regularization techniques; in this analysis, a Gauss-Newton method was used for minimization and Tikhonov regularization was used to damp oscillations.

V. Experimental Validation

Experimental measurements were used to validate the hot-wall heat flux reconstruction algorithm and compare its performance against FIAT_Opt. In all scenarios, measurements were generated from the MEDLI2 sensor suite or representative sensor configurations. A basis function order of $N = 12$ and regularization coefficient values of $\lambda_2 = 1 \times 10^6$ and $\lambda_2^{(0)} = 1 \times 10^9$ were used in the reconstruction algorithm for all scenarios. The algorithm was used to reconstruct the transient surface heating on panel arc-jet test articles from the MEDLI2 material response model development and Do-No-Harm test campaigns, allowing for comparisons of the reconstructed heating conditions against calibrated tunnel conditions. The reconstruction algorithm was also applied to the Mars 2020 backshell temperature and heat flux measurements to reconstruct the aeroheating environment at the surface of the spacecraft during atmospheric entry. The reconstruction algorithm was then leveraged to perform an uncertainty quantification of the reconstructed Mars 2020 atmospheric entry heat pulse. Uncertainty quantification results were compared with a prior machine learning approach for the peak heating region.

A. MEDLI2 Material Response Model Development and Do-No-Harm Test Campaigns

During the development and qualification of the MEDLI2 sensor suite and TPS architecture used on the Mars 2020 spaceflight mission, numerous panel arc-jet tests were performed in the Panel Test Facility (PTF) at NASA Ames. PTF test campaign 162 consisted of four SLA-561V panels instrumented with a TC plug, total heat flux sensor, and radiometer [6, 20] (Fig. 3). The TC plug and heat flux sensor were positioned in an arrangement analogous to the collocated MTB01/MTB07 sensor pair on the Mars 2020 backshell and sampled at a rate of 20 Hz (downsampled to 10 Hz in the reconstruction algorithm). TPS test panels were coated with a white silicone spray, except for within a 5 cm radius of each sensor, to mimic the Mars 2020 backshell configuration (Fig. 3). Nominal test conditions are presented in [20] and shown in Table 1. The first two tests represent low heating conditions, whereas the latter two tests represent high heating conditions.

Reconstructed heat flux profiles are shown in Fig. 4 for the low heating (Fig. 4a and 4b) and high heating (Fig. 4c and 4d) test conditions. The blue line in each plot represents the net hot-wall heat flux q_{HW} conducted into the solid and the orange line represents the incident heat flux from the arc-jet test environment q_{inc} (Eq. (16)). Reconstructed heat flux profiles using the hot-wall heat flux reconstruction algorithm are shown as solid lines and those using FIAT_Opt are shown using dashed lines.

Table 1 Panel arc-jet test campaign 162 run parameters [20].

Test	Target Adiabatic-Wall Heat Flux (W/cm^2)	Target Cold-Wall Heat Flux (W/cm^2)	Steady Test Duration (s)
1 & 2	4.3	5.4	63
3 & 4	8.6	9.7	25

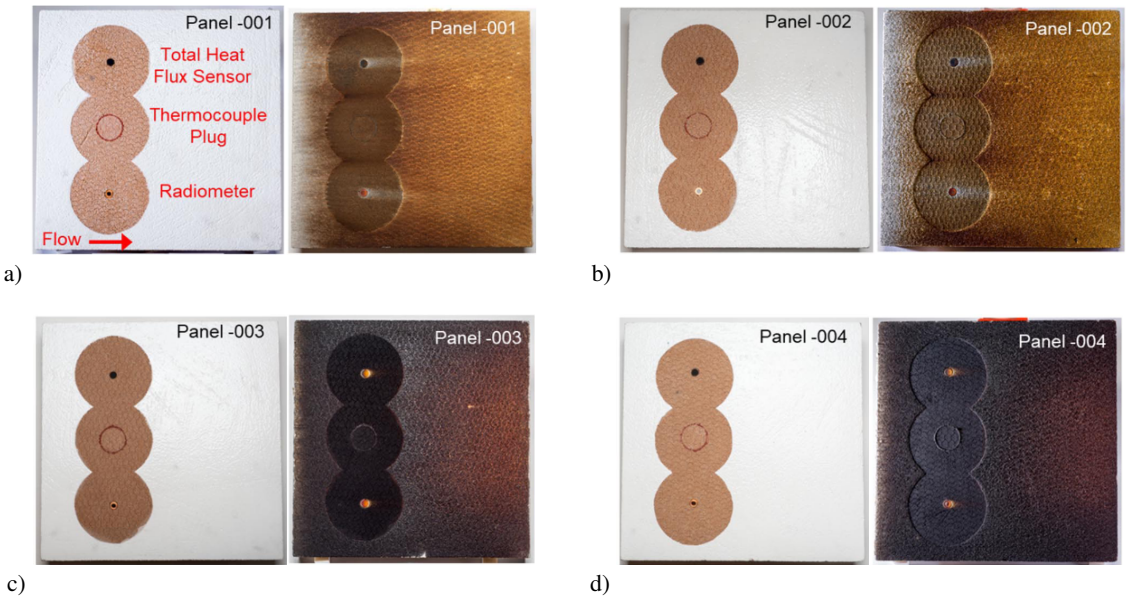

Fig. 3 Panel arc-jet test campaign 162 test articles before (left) and after (right) arc-jet exposure [6]. a) Test 1. b) Test 2. c) Test 3. d) Test 4.

Multiple regions are evident in Fig. 4, including the tunnel startup, test-article insertion, steady test period, test-article extraction, and cool down phases. Most critical is the performance of the hot-wall heat flux reconstruction algorithm during the steady test period, which begins at approximately t = 50 s and ends with a sharp drop in the incident heating upon test-article extraction. Throughout the steady test period, the net hot-wall heat flux decreases with time for all test scenarios as the TPS surface approaches an adiabatic-wall condition ($q_{HW} = 0$). The reconstruction algorithm predicts the net hot-wall heat flux to within 0.1 W/cm^2 (14%) and 0.3 W/cm^2 (26%) of FIAT_Opt for the low and high heating scenarios, respectively, during the steady test period. Over the same period, the incident heat flux, representative of the target heating conditions, is predicted to within 0.16 W/cm^2 (3.3%) and 0.6 W/cm^2 (6%) of FIAT_Opt for the low and high heating scenarios, respectively. The larger discrepancy between solutions from the two methods in the high heating scenario is attributed to the effects of through-thickness pyrolysis in the TPS, as suggested by the substantial post-test surface char observed in the high heating scenarios (Fig. 3c and 3d) and as predicted by the FIAT_Opt results. Substantial pyrolysis would alter the material properties and heat conduction within the TPS; while FIAT_Opt accounts for this, the hot-wall heat flux reconstruction algorithm currently neglects the effects of any through-thickness pyrolysis and material decomposition, and only assumes char formation at the TPS surface for the calculation of the emissivity.

In the low heating scenarios, both methods predict the incident heat flux within the target cold-wall and adiabatic-wall bounds during the steady test period. In the high heating scenarios, both methods overpredict the target cold-wall heating conditions by up to 15%. It should be noted, however, that the stated uncertainty for the calibrated PTF cold-wall heat flux is ±15% [21]. Considering expanded cold-wall and adiabatic-wall bounds due to facility calibration uncertainties, both reconstruction methods adequately predict the incident heating conditions in the high heating scenarios.

The largest discrepancy between reconstructions from both approaches occurs prior to the cool-down phase, when the

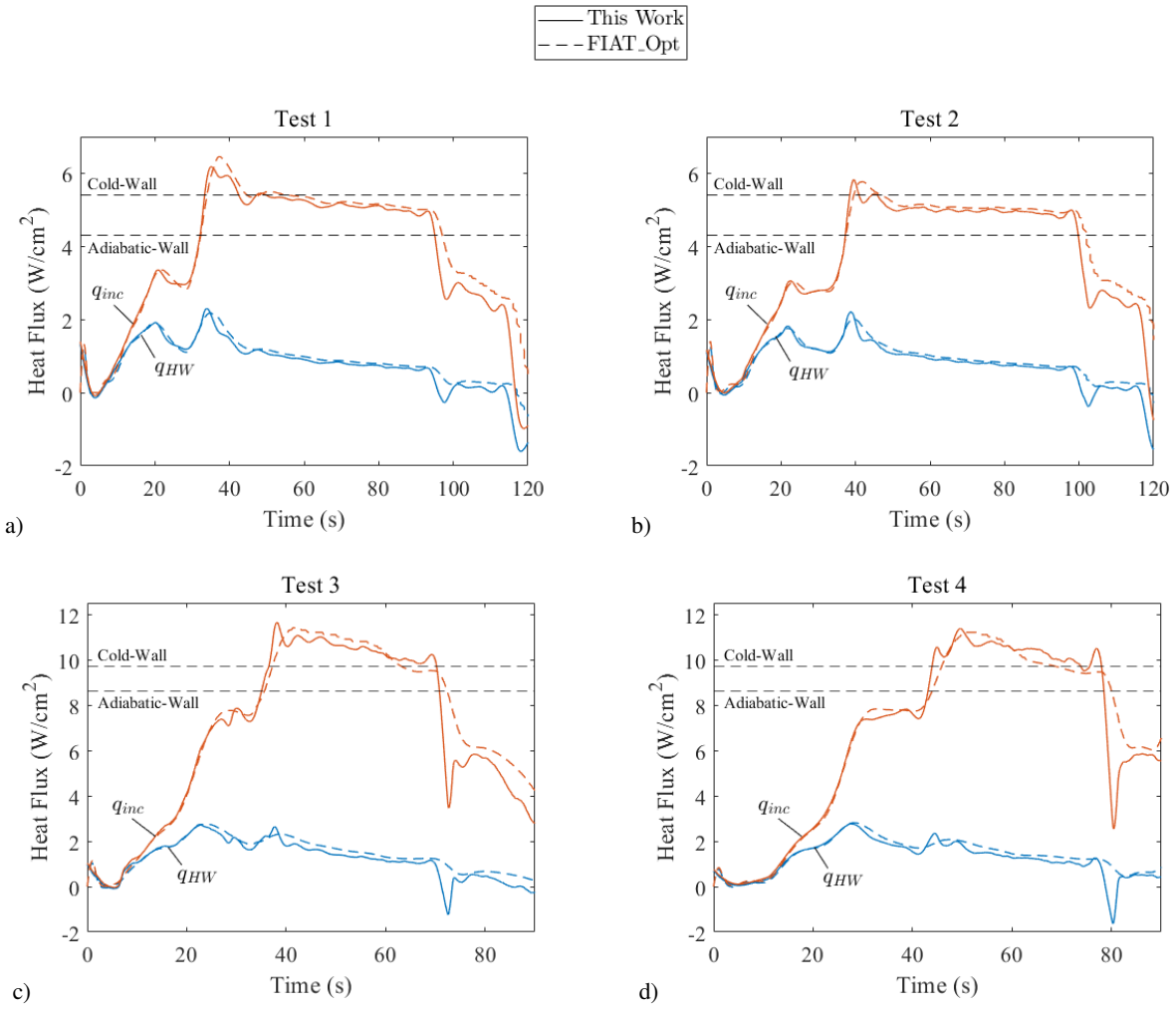

Fig. 4 Reconstructed net hot-wall (blue) and incident (orange) heating results for instrumented arc-jet test articles from PTF test campaign 162 a) Test 1, b) Test 2, c) Test 3, and d) Test 4. The solid series represent results from the hot-wall heat flux reconstruction algorithm and the dashed series represent results from FIAT_Opt. In each plot, the black dashed lines represent the target cold-wall or adiabatic-wall heat flux, labeled respectively.

panel test-article is extracted from the direct flow path. In all scenarios, the hot-wall heat flux reconstruction algorithm predicts a brief, negative net hot-wall heat flux as the heat flux incident on the test article is quickly reduced. This phenomena is physical: near the end of the steady test period, the TPS surface converges towards a true adiabatic-wall condition, where the incident heating is balanced by the radiative emission from the hot TPS surface. In this state, any decrease in the incident heat flux will result in a negative net hot-wall heat flux on the surface. This feature is not resolved by FIAT_Opt (Fig. 4, dashed lines). In general, the hot-wall heat flux reconstruction algorithm resolves sharper features in the reconstructed surface heating conditions compared to FIAT_Opt, notably during highly transient heating regions, such as when the test article is positioned in and out of the flow. This robust sharp feature resolution is likely due to the use of a regularization surrogate in the current approach (i.e., the collocated heat flux sensor), which has been shown previously to preserve highly varying solution features compared to conventional regularization approaches, such as Tikhonov regularization, as utilized by FIAT_Opt [8].

B. Mars 2020 Aerothermal Environment Reconstruction

The hot-wall heat flux reconstruction algorithm was used to reconstruct the atmospheric entry aeroheating on the Mars 2020 backshell at the MTB01/MTB07 and MTB02/MTB08 sensor pair locations (Fig. 1). In this analysis, the reconstructed net hot-wall and incident heat flux using the hot-wall heat flux reconstruction algorithm are compared with prior FIAT_Opt results from the post-flight reconstruction of the Mars 2020 atmospheric entry environment [5].

Reconstructed net hot-wall and incident heat flux profiles are shown in Fig. 5 for both sensor pairs. Consistent with prior analysis, the MTB02/MTB08 sensor pair on the leeward-side experienced the highest incident heating on the backshell, with a reconstructed peak heat flux of 4.96 W/cm^2 (calculated using the current approach). For both sensor pairs, a bimodal peak region is present in the reconstructed incident heating, suggesting the presence of separate radiative and convective peak heating regimes.

The hot-wall heat flux reconstruction algorithm predicts a very similar net hot-wall heat flux profile compared with FIAT_Opt (blue curves in Fig. 5), with the peak values recovered to within 0.07 W/cm^2 (4%) and 0.03 W/cm^2 (1%) for the MTB01/MTB07 and MTB02/MTB08 sensor pairs, respectively. At the peak incident heating time, the hot-wall heat flux reconstruction algorithm overpredicts the FIAT_Opt-generated incident heat flux (orange curves in Fig. 5) by 0.3 W/cm^2 (10%) and 0.3 W/cm^2 (6%) for the MTB01/MTB07 and MTB02/MTB08 sensor pairs, respectively. Following the peak heating time, reconstructed net hot-wall and incident heating conditions decay at a faster rate compared with those generated using FIAT_Opt and reach a larger negative peak value, notably for the MTB02/MTB08 sensor pair.

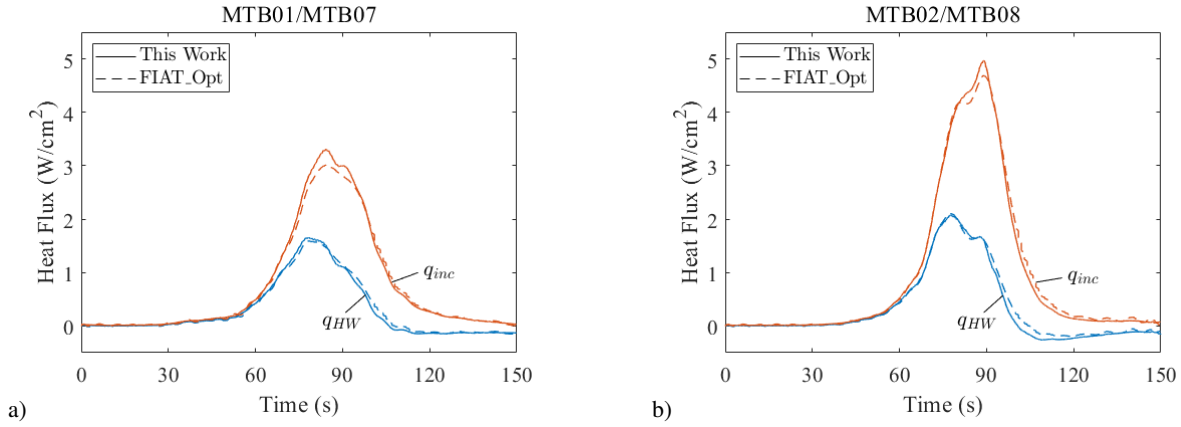

Fig. 5 Reconstructed heat flux profiles from the Mars 2020 backshell. a) Results from the MTB01/MTB07 sensor pair. b) Results from the MTB02/MTB08 sensor pair.

The higher estimated peak incident heating for both sensor pairs using the hot-wall heat flux reconstruction algorithm is correlated with a higher reconstructed TPS surface temperature. Reconstructed surface temperature profiles using the reconstruction algorithm and FIAT_Opt are shown in Fig. 6. For both sensor pairs, the reconstruction algorithm overpredicts the surface temperature near the peak heating time. At their respective peaks, the surface temperature is overpredicted by 25 K and 17 K for the MTB01/MTB07 and MTB02/MTB08 sensor pairs, respectively. Because the radiative heat flux emitted by the hot TPS surface scales with $\tilde{T}_s^4$, small discrepancies in the estimated surface temperature

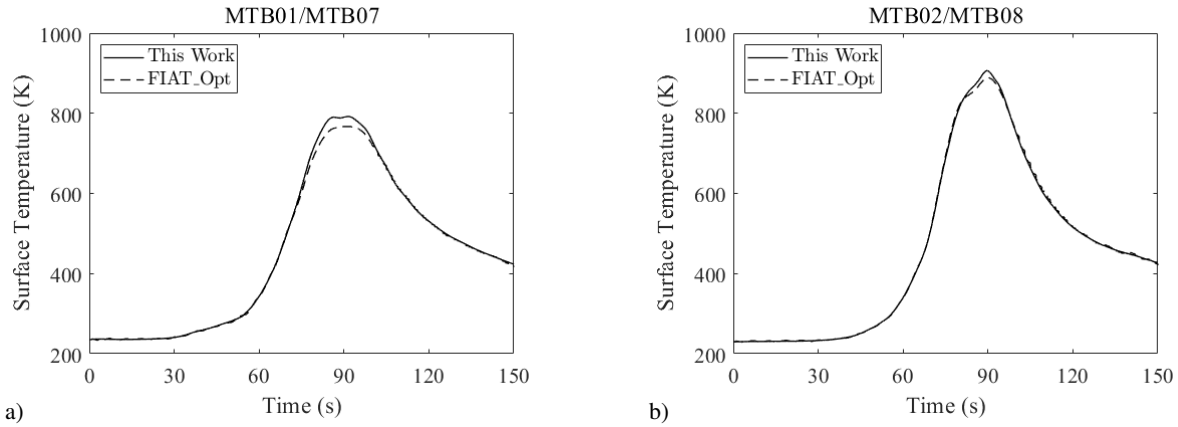

Fig. 6 Reconstructed surface temperatures from the Mars 2020 backshell. a) Results from the MTB01/MTB07 sensor pair. b) Results from the MTB02/MTB08 sensor pair.

lead to larger differences in the estimated incident heat flux q_{inc}. It is also worth noting again that the hot-wall heat flux reconstruction algorithm does not include the effects of through-thickness material decomposition and pyrolysis in the Green's function formulation. These mechanisms are expected to lead to a decrease in the surface temperature rise, and therefore a decrease in the magnitude of q_{inc} and better agreement with FIAT_Opt. Implementation of these effects in the reconstruction algorithm will be the subject of a future publication. Nonetheless, these results demonstrate that the Green's function-based reconstruction algorithm can generally capture the relevant heat conduction phenomena in an atmospheric entry scenario to within 10% of state-of-the-art methods and, notably, can compute such in three orders of magnitude less time.

VI. Uncertainty Quantification and Variance-Based Sensitivity Analysis

In the post-flight reconstruction of the Mars 2020 atmospheric entry environment, Monte Carlo analyses were used to determine the overall uncertainty of the reconstructed surface heating conditions. While Monte Carlo simulations are sufficient to estimate the overall reconstruction uncertainty, more detailed analyses are required to decompose the individual contributions of various input parameters to the overall output uncertainty. These analyses are critical to guide materials characterization efforts and reduce the margins of post-flight reconstructed atmospheric entry environments in the most cost-effective manner. Variance-based sensitivity analyses—such as the calculation of first order or total Sobol indices—are often used to quantify input parameter uncertainty contributions [22]. As a metric, the total Sobol index of an input parameter is defined as the remaining model output variance when all other parameters are fixed, normalized by the total model variance [23]. More generally, the total Sobol index of a parameter can be considered as the fractional contribution of the uncertainty of that parameter to the total model output uncertainty. Due to the computational cost of such analyses, however, calculating total Sobol indices organically using FIAT_Opt simulations is not a practical endeavor. In prior work, a machine learning-based approach was implemented to overcome the computational burden: using a limited set of Monte Carlo simulations, a surrogate model was trained to predict the peak heat flux and heat load at each thermocouple plug location [5] and allowed for the calculation of total Sobol indices with respect to these two features. While this technique was able to generate some insight into the major contributors to uncertainty in the reconstructed peak heat flux and integrated heat load, it did not give any insight with respect to other periods or features throughout the entry heat pulse.

In this section, the hot-wall heat flux reconstruction algorithm is used to calculate the uncertainty of the reconstructed net hot-wall and incident heat flux, as well as total Sobol indices for each input parameter throughout the entire atmospheric entry flight duration. Input parameter uncertainty distributions for the Mars 2020 flight lot backshell TPS and the embedded temperature probe are tabulated in Table 2. Uncertainty distributions in Table 2 are normalized by the mean value, unless otherwise noted, and are representative of those used in prior MEDLI2 post-flight analyses [5]. The variations in virgin and char densities were coupled using a single scaling distribution. For material properties that are bounded, such as emissivity, a truncated normal distribution was used to avoid non-physical inputs.

Table 2 Input uncertainty scaling parameters from [5]. Both uniform (U) and normal (N) distributions were used in this analysis.

	$\rho_v = \rho_c$	C_p	ϵ_v	ϵ_c	k	x_T
Distribution	U	N	N*	N*	N	N
$2\sigma/\mu$	$\pm 0.018^{\dagger}$	0.15	0.15	0.15	0.13	0.0076 cm‡

* Truncated normal distribution
† Upper/lower bounds
‡ Not normalized by mean

Monte Carlo simulations (5000 samples) were used to compute the overall uncertainty of the reconstructed heating values. Resulting distributions of the reconstructed net hot-wall and incident heat flux for each sensor pair are shown in Fig. 7. In Fig. 7, the overall solution distribution is represented as a mean solution with a 95% confidence interval envelope ($\pm 1.96\sigma$) for both the net hot-wall (blue) and incident (orange) heat flux. To obtain a faster convergence, the input temperature and heat flux measurements were downsampled from 8 Hz and 16 Hz, respectively, to 4 Hz. In addition, input parameter uncertainty distributions were sampled using quasi-random Latin Hypercube sampling. In preliminary testing, sampling the measurements at a rate of 8 Hz resulted in a computation time of 9 s for each reconstruction, on average. Downsampling by a factor of two, reconstructed heat flux profiles converged in 2-3 s on average, or four times as fast. Reconstructed net hot-wall and incident heat flux values using downsampled measurements were within 5% of their natively sampled counterparts within the most relevant heating region from $t = 70$ s to $t = 100$ s.

At the peak heat time, the 95% confidence interval for the reconstructed incident heat flux spans 1.5 W/cm^2 for the MTB01/MTB07 sensor pair (Fig. 7a) and 2.3 W/cm^2 for the MTB02/MTB08 sensor pair (Fig. 7b), in good agreement with prior analysis [5]. For both sensor pairs, the largest variation in both the reconstructed net hot-wall and incident heating values coincided with the respective peak heating times.

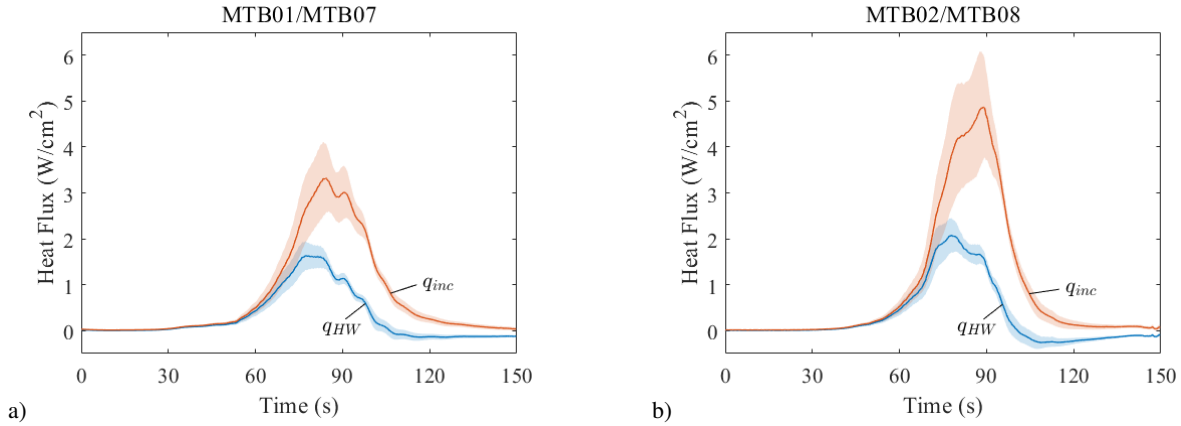

Fig. 7 Results from Monte Carlo simulations for the reconstructed surface heating conditions for the a) MTB01/MTB07 and b) MTB02/MTB08 sensor pairs. The solid line represents the mean solution. The shaded envelope represents a 95% confidence interval.

Next, total Sobol indices were calculated to determine the individual contributions of the input parameter uncertainties to the total uncertainty of the reconstructed heating values in Fig. 7. To calculate the total Sobol indices S_T for each input parameter i, the Monte Carlo estimator proposed in [24] was employed

$$S_{T,i} = \frac{1}{2} \frac{\sum_{j=1}^{N_s} \left[q(A)_j - q(A_B^{(i)})_j \right]^2}{\sum_{j=1}^{N_s} \left[q(A)_j - q_0 \right]^2} \tag{19}$$

In Eq. (19) N_s represents the number of samples per input parameter, q represents the model output, either the net

hot-wall or incident heat flux, and q_0 is the mean solution. The variables A and $A_B^{(i)}$ are sampling matrices with dimensions of $N_s \times k$, where k is the number of uncertainty parameters. The matrix $A_B^{(i)}$ is constructed by replacing column i in matrix A with column i in matrix B, where B is an independent sampling matrix with the same dimensions as A. Thus, for N_s samples, $N_s \times (k+1)$ independent reconstructions are required.

Total Sobol indices were calculated at each timestep during the entry heat pulse for the reconstructed net hot-wall and incident heat flux for both sensor pairs using $N_s = 5000$ samples per input parameter in Table 2 ($k = 6$). Convergence plots of the peak heating total Sobol indices for the MTB02/MTB08 sensor pair are shown in Fig. 8. For both the reconstructed net hot-wall and incident heat flux, total Sobol indices at the peak heating time were fully converged after approximately $N_s = 3000$ samples. Total Sobol indices for the reconstructed net hot-wall heat flux are plotted in Fig. 9 and 10 for the MTB01/MTB07 and MTB02/MTB08 sensor pairs, respectively. Likewise, total Sobol indices for the reconstructed incident heat flux are plotted in Fig. 11 and 12 for the MTB01/MTB07 and MTB02/MTB08 sensor pairs, respectively. In each plot, labeled datapoints at the respective peak heating times represent the total Sobol indices calculated using the machine learning approach described in [5].

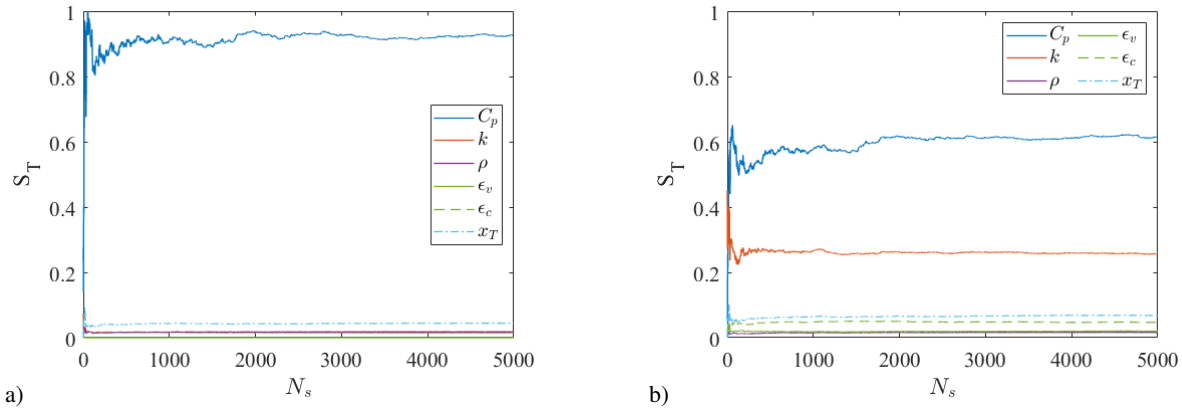

Fig. 8 Convergence plots of the peak heating total Sobol index for the a) net hot-wall heat flux and b) incident heat flux for the MTB02/MTB08 sensor pair.

For each sensor pair, total Sobol indices for the reconstructed net hot-wall heat flux (Fig. 9 and 10) remained relatively constant until the peak heating region, with the reconstruction uncertainty dominated by the uncertainty in specific heat. Near the peak net hot-wall heating time, the uncertainty in specific heat contributes over 90% of the reconstruction uncertainty. At peak q_{HW}, total Sobol indices calculated using the current approach show substantial agreement with those calculated using the prior machine learning approach for both sensor pairs (solid circles in Fig. 9 and 10). Following the peak heating region, total Sobol indices vary drastically. As the heat pulse subsides, the thermal conductivity total Sobol index increases substantially, up to 0.95 at $t = 94$ s for both sensor pairs, and the uncertainty in the specific heat is no longer the primary driver of the reconstruction uncertainty. Between the peak net hot-wall heating time and $t = 90$ s, an additional spike, and subsequent drop, in the thermal conductivity Sobol index occurs for the MTB01/MTB07 sensor pair (Fig. 9). This feature is not present in the results from the MTB02/MTB08 sensor pair, in which the specific heat uncertainty dominates the total output uncertainty until $t = 90$ s (Fig. 10).

The strong dependence of the output uncertainty on the uncertainty of the specific heat for the reconstructed net-hot wall heat flux can be explained by considering how specific heat, or thermal mass ($\rho_s C_p$), dominates the transient response characteristics of the TPS thermal history near the embedded temperature probe (Eq. (1)). The effect of thermal mass is to impart a delay into the temperature response when the TPS is subject to transient surface heating conditions. Up to peak heating, the heat flux boundary condition is increasing rapidly, such that any variation in the delay introduced in the reconstruction relative to the mean solution will induce the most significant variation in the model output. The large increase in the thermal conductivity total Sobol index for the reconstructed net hot-wall heat flux following the peak heating region can potentially be explained by considering the heat soak within the TPS. Due to the highly insulating properties of the Mars 2020 backshell, the short entry heat pulse likely achieved a very shallow thermal penetration depth, leading to significant thermal energy storage near the TPS surface in the form of a hot layer. After the regime of maximum heating, the rate of heat dissipation from the near-surface hot region into the inner TPS

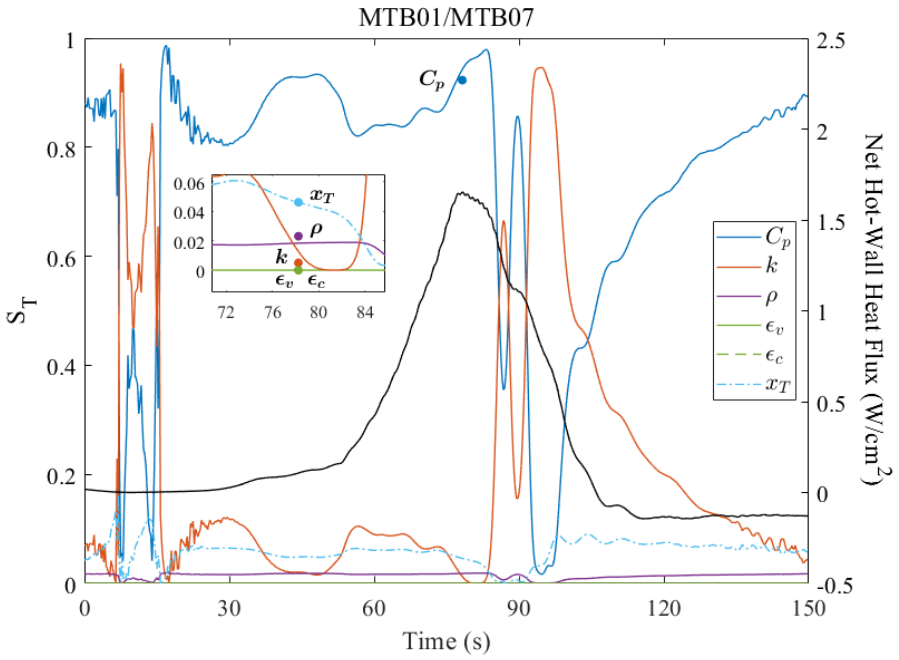

Fig. 9 Total Sobol index calculations for the reconstructed net hot-wall heat flux for the MTB01/MTB07 sensor pair. Labeled datapoints at the respective peak heating times are the total Sobol indices calculated using the machine learning approach described in [5]. The solid black line is the nominal reconstructed net-hot wall heat flux solution from Section V.B. Inset: Magnified region for the total Sobol indices at the peak heating time.

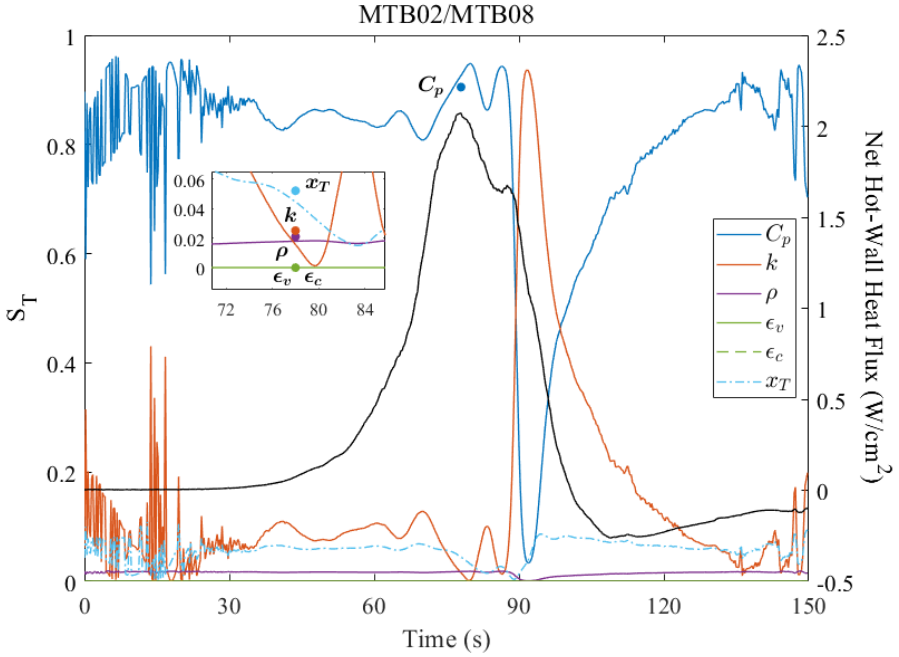

Fig. 10 Total Sobol index calculations for the reconstructed net hot-wall heat flux for the MTB02/MTB08 sensor pair. Labeled datapoints at the respective peak heating times are the total Sobol indices calculated using the machine learning approach described in [5]. The solid black line is the nominal reconstructed net-hot wall heat flux solution from Section V.B. Inset: Magnified region for the total Sobol indices at the peak heating time.

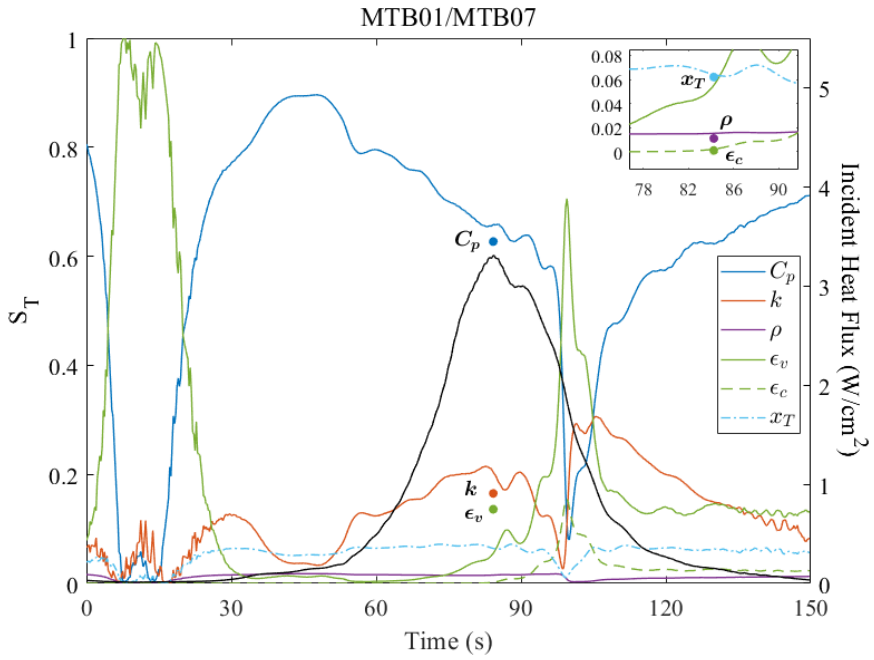

Fig. 11 Total Sobol index calculations for the reconstructed incident heat flux for the MTB01/MTB07 sensor pair. Labeled datapoints at the respective peak heating times are the total Sobol indices calculated using the machine learning approach described in [5]. The solid black line is the nominal reconstructed incident heat flux solution from Section V.B. Inset: Magnified region for the total Sobol indices at the peak heating time.

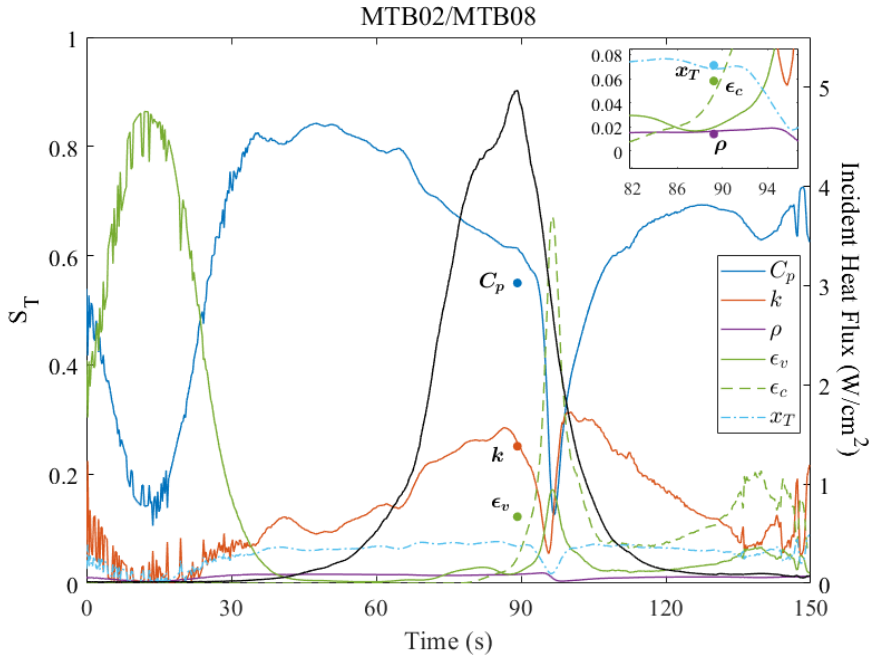

Fig. 12 Total Sobol index calculations for the reconstructed incident heat flux for the MTB02/MTB08 sensor pair. Labeled datapoints at the respective peak heating times are the total Sobol indices calculated using the machine learning approach described in [5]. The solid black line is the nominal reconstructed incident heat flux solution from Section V.B. Inset: Magnified region for the total Sobol indices at the peak heating time.

will occur proportional to the thermal conductivity, leading to a larger propagation of thermal conductivity uncertainty into the total output uncertainty. It is also worth highlighting the intermediate peak in the thermal conductivity total Sobol index for the MTB01/MTB07 sensor pair at $t = 86$ s (Fig. 9), which coincides with an inflection point in the incident heating profile (Fig. 5a). This behavior suggests two distinct periods of heat soak and through-thickness dissipation within the TPS at the MTB01/MTB07 sensor pair location, and contrasts with the continuous monotonic heat soak experienced by the TPS at the MTB02/MTB08 sensor pair location. For both sensor pairs, as the hot layer cools, the reconstruction uncertainty becomes less sensitive to variations in the thermal conductivity, leading to a steady decay of the thermal conductivity total Sobol index with time.

For both sensor pairs, the uncertainty of the reconstructed incident heat flux (Fig. 11 and 12) up to peak heating is dominated by the uncertainty in the specific heat, albeit to a lesser extent than the reconstructed net hot-wall heat flux. At the peak incident heat flux, the uncertainty in the specific heat contributes approximately 60% of the output uncertainty whereas the thermal conductivity contributes approximately 20% of the output uncertainty, both of which are in good agreement with results from the prior machine learning approach. Other total Sobol indices at the peak incident heating time are also in good agreement with the prior approach, with the exception of the virgin emissivity total Sobol index for the MTB02/MTB08 sensor pair (Fig. 12). This discrepancy is primarily attributed to the accelerated formation of char on the surface caused by the over-prediction of the TPS surface temperature, compared with FIAT_Opt (Fig. 6). Due to the discrepancies in the reconstructed surface char state between the two approaches, uncertainties in the virgin and char properties propagate differently into the total output uncertainty via the composite emissivity (Eq. (17)).

Immediately following peak incident heating, total Sobol indices for both the specific heat and thermal conductivity drop rapidly, and the virgin and char emissivity total Sobol indices rise. For the MTB01/MTB07 sensor pair, the virgin emissivity uncertainty begins to dominate the total output uncertainty, with a total Sobol index of 0.7 at $t = 100$ s. For the MTB02/MTB08 sensor pair, the char emissivity uncertainty begins to dominate the total output uncertainty, with a similar total Sobol index of 0.7 at $t = 100$ s. Following their respective peaks, the emissivity total Sobol indices decay quickly and the specific heat and thermal conductivity total Sobol indices increase.

The incident heating results (Fig. 11 and 12) show a similar trend as the net hot-wall heating results (Fig. 9 and 10), where the uncertainty in heat capacity is the main driver of the reconstruction uncertainty up to peak heating. The larger uncertainty contribution of the thermal conductivity up to peak heating for the reconstructed incident heat flux is attributed to the effects of radiative emission at the TPS surface: while the transient thermal response characteristics of the TPS may be more strongly coupled with its thermal mass, the magnitude of the temperature rise at the surface, which contributes to the radiative emission by $\tilde{T}_s^4$, is dominated more-so by its thermal conductivity. Thus, the variation in the reconstructed incident heat flux becomes sensitive to the variation in the thermal conductivity. Following peak heating, the corresponding dominance of the virgin or char emissivity uncertainty on the reconstructed incident heating uncertainty at $t = 100$ s (Fig. 11 and 12) is attributed to the estimated char state at the TPS surface: due to the increased heating at the MTB02/MTB08 sensor pair location, the surface of the MTB02 TC plug at $t = 100$ s is estimated to be closer to a fully charred state, whereas the MTB01 TC plug surface is estimated to be only slightly pyrolyzed, resulting in a different sensitivity to variation in virgin and char properties.

For the Mars 2020 backshell TPS, reductions in the uncertainty of the specific heat, thermal conductivity, and emissivity will yield the most effective reduction in the overall reconstructed aeroheating uncertainty. These results, however, highlight how the uncertainty margins attributed to post-flight aerothermal environment reconstructions are dynamically sensitive to variation in the different input parameters throughout the entry heat pulse. While the peak heating total Sobal indices expose the input parameters which drive the uncertainty of the aeroheating reconstruction within the region of the largest heat flux and the largest reconstruction uncertainty, they are not necessarily applicable to other regions which are also considered in the design and sizing of TPS. This is a significant consideration when adapting uncertainty quantification efforts to other missions, such as Dragonfly, which utilizes a similar TPS architecture to Mars 2020 but features a prolonged convective cooling phase during atmospheric entry [25].

VII. Conclusion

A Green's function-based hot-wall heat flux reconstruction algorithm demonstrated accurate and efficient computation of the surface heating conditions on spacecraft TPS during atmospheric entry. The algorithm directly computes the net hot-wall heat flux conducted into the TPS solid using a Green's function IHT formulation with measurement inputs from embedded temperature probe and heat flux sensor instrumentation. To isolate the combined radiative and convective heating absorbed by the TPS, the algorithm corrects the net hot-wall heat flux with the radiative emission from the hot-wall TPS surface. By leveraging a mesh-less heat conduction model, the reconstruction algorithm can recover the

surface heating conditions from input measurements in three orders of magnitude less time than current state-of-the-art IHT codes for entry spacecraft applications. The performance of the algorithm was compared against the current state-of-the-art IHT methodology for spacecraft TPS, FIAT_Opt. Using temperature and heat flux measurements from sensors embedded in arc-jet ground test articles from PTF test campaign 162 at NASA Ames, the hot-wall heat flux reconstruction algorithm computed the incident heating values from the test environment to within 6% of FIAT_Opt during steady test conditions. Applied to measurements from the MEDLI2 instrumentation suite aboard the Mars 2020 atmospheric entry vehicle, the hot-wall heat flux reconstruction algorithm calculated the net hot-wall and incident heating conditions on the backshell in close agreement with FIAT_Opt throughout the entire flight duration. The reconstruction algorithm recovered the peak net hot-wall and incident heating values to within 4% and 10%, respectively, of FIAT_Opt. Calculation of the total Sobol indices of the reconstruction algorithm input parameters with respect to the net hot-wall and incident heat flux highlighted how the Mars 2020 flight lot uncertainties of the specific heat, thermal conductivity, and surface emissivity were dominant drivers of the total reconstruction uncertainty at different times during the entry heat pulse, with excellent agreement obtained between the current approach and a prior machine learning approach at the peak heating times. A juxtaposition of the full-flight total Sobol indices for the MTB01/MTB07 and MTB02/MTB08 sensor pairs highlighted how the uncertainty of virgin and char material properties propagate differently into the total reconstruction uncertainty depending on the estimated char state of the TPS.

These results establish Green's functions and sensor fusion-based regularization methods as promising techniques for the analysis of atmospheric entry spacecraft aeroheating. In future work, the hot-wall heat flux reconstruction algorithm will be adapted to include the effects of pyrolysis, material decomposition, and gas transport in the Green's function formalism. The algorithm will be extended to reconstruct the global TPS surface heating and aeroheating environment at all locations instrumented with thermocouples on the Mars 2020 backshell, including at locations without a collocated heat flux sensor. Overall, access to more efficient reconstruction techniques will help to reduce sizing margins, improve material models, and guide TPS characterization efforts with a substantially reduced cost compared to current methodologies.

Acknowledgments

This work was supported by a NASA Space Technology Graduate Research Opportunity (grant 80NSSC23K1201). The authors would like to acknowledge Antonella Alunni, Ruth Miller, Quincy McKown, and Sam Preece for their comments and reviews of this work.

References

[1] White, T. R., Mahzari, M., Miller, R. A., Tang, C. Y., Karlgaard, C. D., Alpert, H., Wright, H. S., and Kuhl, C., "Mars Entry Instrumentation Flight Data and Mars 2020 Entry Environments," *AIAA SCITECH 2022 Forum*, American Institute of Aeronautics and Astronautics, San Diego, CA & Virtual, 2022. https://doi.org/10.2514/6.2022-0011.

[2] Swanson, G., Kazemba, C., Miller, R. A., Alpert, H., Williams, J., Stephen, H., and Cheatwood, N., "Overview and Performance of the LOFTID Instrumentation Suite," *AIAA SCITECH 2024 Forum*, American Institute of Aeronautics and Astronautics, Orlando, FL, 2024. https://doi.org/10.2514/6.2024-1712.

[3] Gülhan, A., Thiele, T., Siebe, F., Kronen, R., and Schleutker, T., "Aerothermal Measurements from the ExoMars Schiaparelli Capsule Entry," *Journal of Spacecraft and Rockets*, Vol. 56, No. 1, 2019, pp. 68–81. https://doi.org/10.2514/1.A34228.

[4] Mahzari, M., Braun, R. D., White, T. R., and Bose, D., "Inverse Estimation of the Mars Science Laboratory Entry Aeroheating and Heatshield Response," *Journal of Spacecraft and Rockets*, Vol. 52, No. 4, 2015, pp. 1203–1216. https://doi.org/10.2514/1.A33053.

[5] Alpert, H. S., Saunders, D. A., Mahzari, M., Monk, J. D., White, T. R., and West, T. K., "Inverse Estimation and Sensitivity Analysis of Mars 2020 Entry Aeroheating Environments," *Journal of Spacecraft and Rockets*, Vol. 60, No. 3, 2023, pp. 899–911. https://doi.org/10.2514/1.A35571.

[6] Miller, R. A., Tang, C. Y., Santos, J. A. B., White, T. R., and Cruden, B. A., "Aftbody Heat Flux Measurements During Mars 2020 Entry," *Journal of Spacecraft and Rockets*, Vol. 61, No. 2, 2024, pp. 369–382. https://doi.org/10.2514/1.A35783.

[7] Oliver, B., and Amar, A. J., "Inverse Heat Conduction Methods in the CHAR Code for Aerothermal Flight Data Reconstruction," *46th AIAA Thermophysics Conference*, American Institute of Aeronautics and Astronautics, Washington, D.C., 2016. https://doi.org/10.2514/6.2016-3384.

[8] McAfee, K., Alpert, H., Sunderland, P., and Rabin, O., "A Green's Function Sensor Fusion Approach for Evaluating Spacecraft Entry Heating From On-Board Thermal Instrumentation," *AIAA AVIATION FORUM AND ASCEND 2024*, American Institute of Aeronautics and Astronautics, Las Vegas, NV, 2024. https://doi.org/10.2514/6.2024-4033.

[9] Cole, K., Beck, J., Haji-Sheikh, A., and Litkouhi, B., *Heat Conduction Using Greens Functions*, 2nd ed., CRC Press, 2010.

[10] Massa, L., and Schetz, J. A., "Hypersonic Heat Flux Reconstruction with Distributed Temperature Sensors," *Journal of Thermophysics and Heat Transfer*, Vol. 34, No. 2, 2020, pp. 331–346. https://doi.org/10.2514/1.T5778.

[11] Whalen, T. J., Laurence, S. J., Marineau, E. C., and Ozawa, H., "A Green's Function Approach to Heat-Flux Estimation from Temperature-Sensitive Paint Measurements," *Measurement Science and Technology*, Vol. 32, No. 11, 2021, p. 114011. https://doi.org/10.1088/1361-6501/ac16ee.

[12] Mahzari, M., Beck, R., Hwang, H., Monk, J., Morgan, J., Williams, J., and Edquist, K. T., "Development and Sizing of the Mars 2020 Thermal Protection System," *AIAA AVIATION 2022 Forum*, American Institute of Aeronautics and Astronautics, Chicago, IL & Virtual, 2022. https://doi.org/10.2514/6.2022-3951.

[13] Vadasz, P., "Analytical Solution to Nonlinear Thermal Diffusion: Kirchhoff Versus Cole–Hopf Transformations," *Journal of Heat Transfer*, Vol. 132, No. 12, 2010, p. 121302. https://doi.org/10.1115/1.4002325.

[14] Nguyen, N. M., Ruda, M. L., and Massa, L., "Effect of Insulations and Coatings on Hypersonic Heat Flux Reconstruction," *Journal of Thermophysics and Heat Transfer*, Vol. 35, No. 1, 2021, pp. 63–79. https://doi.org/10.2514/1.T5995.

[15] Ma, J., Rokhlin, V., and Wandzura, S., "Generalized Gaussian Quadrature Rules for Systems of Arbitrary Functions," *SIAM Journal on Numerical Analysis*, Vol. 33, No. 3, 1996, pp. 971–996. https://doi.org/10.1137/0733048.

[16] Yang, T. Y., *Finite Element Structural Analysis*, Prentice-Hall, 1986.

[17] Amar, A. J., Oliver, B., Kirk, B., Salazar, G., and Droba, J., "Overview of the CHarring Ablator Response (CHAR) Code," *46th AIAA Thermophysics Conference*, American Institute of Aeronautics and Astronautics, Washington, D.C., 2016. https://doi.org/10.2514/6.2016-3385.

[18] Moyer, C., and Rindal, R., "An Analysis of the Coupled Chemically Reacting Boundary Layer and Charring Ablator: Part 2," Tech. Rep. NASA CR 1061, 1968.

[19] Chen, Y.-K., and Milos, F. S., "Ablation and Thermal Response Program for Spacecraft Heatshield Analysis," *Journal of Spacecraft and Rockets*, Vol. 36, No. 3, 1999, pp. 475–483. https://doi.org/10.2514/2.3469.

[20] Monk, J., Feldman, J. D., Mahzari, M., Santos, J. A., White, T. R., Prabhu, D. K., and Alpert, H., "MEDLI2 Material Response Model Development and Validation," *AIAA SCITECH 2022 Forum*, American Institute of Aeronautics and Astronautics, San Diego, CA & Virtual, 2022. https://doi.org/10.2514/6.2022-0549.

[21] Gokcen, T., and Alunni, A., "On Laminar to Turbulent Transition of Arc-Jet Flow in the NASA Ames Panel Test Facility," *43rd AIAA Thermophysics Conference*, American Institute of Aeronautics and Astronautics, New Orleans, LA, 2012. https://doi.org/10.2514/6.2012-3304.

[22] Sobol, I. M., "Global Sensitivity Indices for Nonlinear Mathematical Models and Their Monte Carlo Estimates," *Mathematics and Computers in Simulation*, Vol. 55, No. 1, 2001, pp. 271–280. https://doi.org/10.1016/S0378-4754(00)00270-6.

[23] Saltelli, A., Annoni, P., Azzini, I., Campolongo, F., Ratto, M., and Tarantola, S., "Variance Based Sensitivity Analysis of Model Output. Design and Estimator for the Total Sensitivity Index," *Computer Physics Communications*, Vol. 181, No. 2, 2010, pp. 259–270. https://doi.org/10.1016/j.cpc.2009.09.018.

[24] Jansen, M. J. W., "Analysis of Variance Designs for Model Output," *Computer Physics Communications*, Vol. 117, No. 1, 1999, pp. 35–43. https://doi.org/10.1016/S0010-4655(98)00154-4.

[25] Stern, E., and Mahzari, M., "Dragonfly TPS Sizing and Analysis," *AIAA SCITECH 2023 Forum*, American Institute of Aeronautics and Astronautics, National Harbor, MD, 2023.